Regulating surface oxygen species on copper (I) oxides via plasma treatment for effective reduction of nitrate to ammonia

Zhiheng Gong [a,1], Wenye Zhong [a,1], Zuyun He [a], Qiuyu Liu [a], Haijun Chen [a], Deng Zhou [b], Nian Zhang [b], Xiongwu Kang [a], Yan Chen [a,*]

[a] School of Environment and Energy, State Key Laboratory of Pulp and Paper Engineering, South China University of Technology, Guangzhou 510006, China
[b] State Key Laboratory of Functional Materials for Informatics, Shanghai Institute of Microsystem and Information Technology, Chinese Academy of Sciences, Shanghai 200050, China

ARTICLE INFO

ABSTRACT

Electrochemical nitrate reduction (NO_3^-RR) to synthesize ammonia is considered to be a promising strategy to enable artificial nitrogen cycle. Great efforts have been devoted to improving the efficiency and selectivity of the electrocatalysts for NO_3^-RR. Herein, we demonstrate that tuning the oxygen chemical environment via Ar plasma treatment is an effective approach to improve the NO_3^-RR activity of Cu_2O. Combining synchrotron-based X-ray absorption spectroscopy and other advanced spectroscopy techniques, we find that plasma treatment can effectively promote the formation of oxygen vacancies and hydroxyl groups on Cu_2O surface. In-situ diffuse-reflectance infrared Fourier transform spectroscopy and density functional theory calculation further reveal that oxygen vacancies and hydroxyl groups facilitate the adsorption of nitrate and proton transfer on the Cu_2O surface, thus leading to improved ammonia selectivity. Our results clarify the critical role of surface oxygen species for NO_3^-RR and can guide the design of other electrocatalysts via surface engineering.

1. Introduction

Ammonia is considered to be one of the most important chemicals because of its critical role in industries such as agricultures and pharmaceuticals. More recently, ammonia has also attracted great attention as promising energy carrier for energy devices due to its high energy density. Ammonia was traditionally synthesized by Haber-Bosch process which required high pressure and energy consumption [1,2]. Using electricity generated by renewable energy to convert nitrate into recyclable ammonia, not only eliminates nitrate pollution in the environment [3–5], but also provides an effective way for energy storage. Compared with the nitrogen reduction reaction, the nitrate reduction reaction (NO_3^-RR) to NH_3 is not limited by the low solubility of N_2 in water environment, and is thermodynamically more favorable because of lower dissociation energy of N=O bond (204 kJ mol^{-1}) than the N≡N (941 kJ mol^{-1}) [6].

Great efforts have been devoted to developing electrocatalysts with high Faradaic efficiency and ammonia selectivity for NO_3^-RR [6–15]. For instance, Wang et al. [8] developed a Cu/organic molecular

coordination catalyst (Cu-PTCDA), which delivered a high Faradaic efficiency of 85.9% for NH_3 synthesis. Zhang et al. reported a series of Co_3O_4 [9], CuO [10] and TiO_2 [11] based electrocatalysts for the conversion of nitrate to ammonia and gave a developmental perspective [12]. Wang et al. designed a Fe single-atom electrocatalyst with a maximum NH_3 Faradaic efficiency of 75% [13]. Li et al. prepared Fe- or Cu-doped carbon-based catalyst, which delivered a 78.4% ammonia Faradaic efficiency [14]. Despite of all these pioneering works, the performance of the electrocatalyst still requires further enhancement for practical applications. The correlation between surface properties and NO_3^-RR activity is still not well-understood.

For transition metal oxide electrocatalysts, while surface metal was traditionally considered to be the active site, anionic species such as anion doping, oxygen vacancy, hydroxyl group, proton on the surface were recently reported to actively participate in surface reactions [16–26]. For instance, Wang et al. [23] reported that oxygen vacancies on the surface of Co_3O_4 led to the formation of Co–OH* intermediate species, which were believed to play a critical role for oxygen evolution reaction (OER). Zhu et al. [18] modulated the proton conductivity of

double perovskite oxides thin film by crystal orientation, and observed strongly modified proton-coupled electron transfer process during OER. Zheng et al. reported that oxygen vacancy-rich surface can regulate the binding affinities of CuO_x to *CO, *COH and *CH_2 intermediates, leading to enhanced CO_2 reduction reaction (CO_2RR) activity [24]. Roldan Cuenya et al. revealed that oxygen species in the surface and subsurface regions of Cu and Cu-derived oxides played a critical role in determining the hydrocarbon selectivity in CO_2RR, which were even more important than the presence of Cu low-index facets [25,26]. All these works demonstrate that tuning surface oxygen species is a potential approach for improving the electrocatalytic activity of transition metal oxide towards NO_3^-RR.

Plasma treatment has been considered as an environmentally friendly and highly efficient technique for surface modification. And this process can be carried out at room temperature without additional chemical reagents [21,25,26]. In this work, we reported a one-step room temperature Ar plasma strategy to regulate the surface oxygen species of Cu_2O electrocatalyst for strongly enhanced NO_3^-RR performance (Fig. 1a). The combination of X-ray photoelectron spectroscopy (XPS)

and synchrotron-based X-ray absorption spectroscopy (XAS) results suggested that abundant oxygen vacancies and surface hydroxyl groups formed on Cu_2O surface after plasma treatment. As a consequence of such changes in surface oxygen species, the Ar plasma-treated Cu_2O nanoparticles exhibited a significant improvement in Faradaic efficiency and conversion rate for NO_3^-RR. Such enhancement in NO_3^-RR activity was attributed to facilitated nitrate adsorption and proton transfer, as revealed by In-situ diffuse-reflectance infrared Fourier transform spectroscopy (DRIFT) and density functional theory (DFT) calculation. Our results demonstrated the critical role of surface oxygen species in determining the NO_3^-RR performance. The methodology in this work can be easily adapted to tune the activity of other electrocatalysts in which oxygen species are involved in the surface reactions.

2. Experimental section

2.1. Chemical reagents

Cupric sulfate anhydrous ($CuSO_4$, 99.0%), ammonium sulfate-[14]N
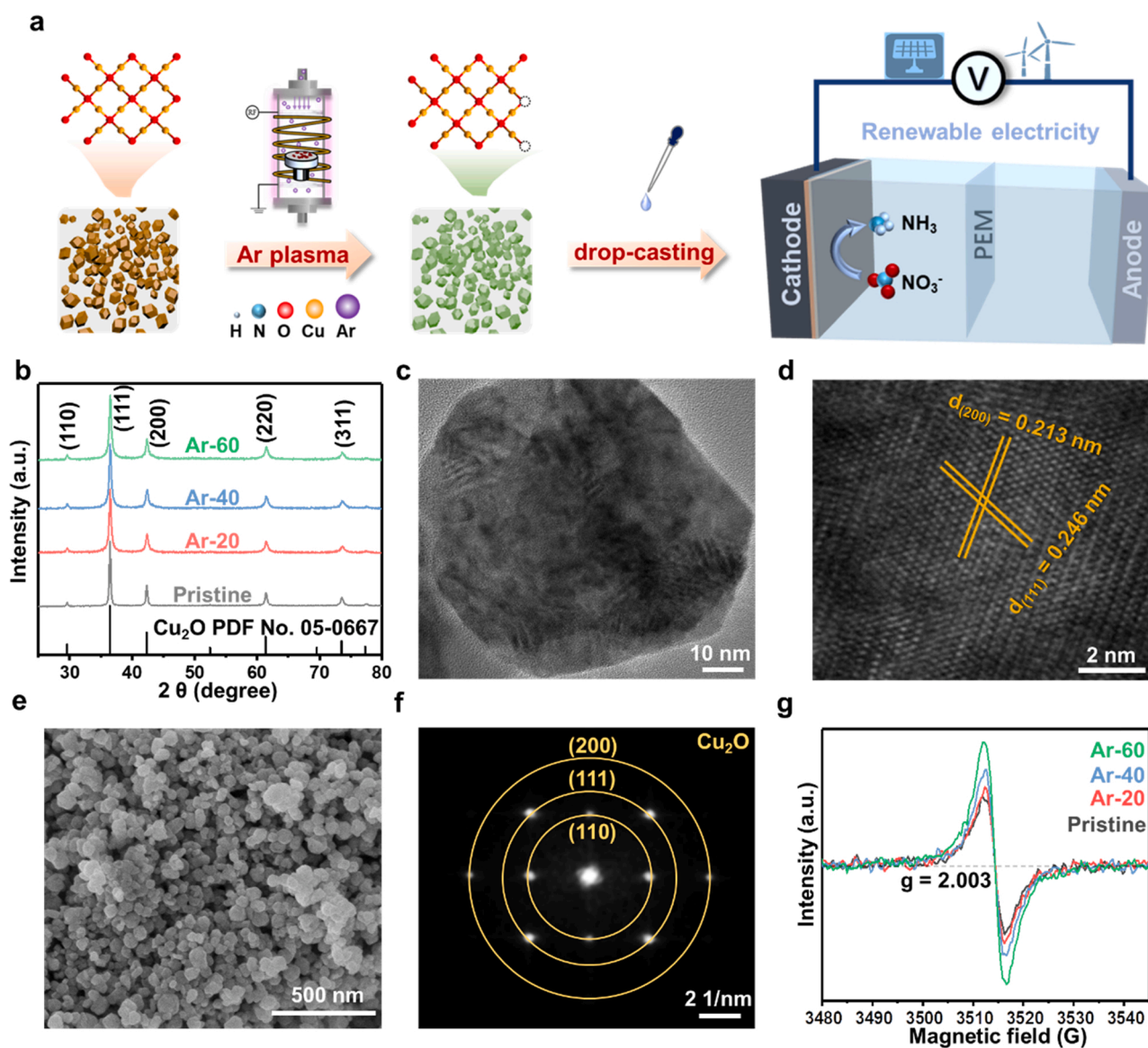

Fig. 1. (a) Schematic illustration for the synthesis process of defective Cu_2O and its application in electrochemical nitrate reduction. (b) XRD patterns of the pristine, Ar-20, Ar-40 and Ar-60. (c–d) HRTEM images with different magnification and (f) the corresponding diffraction pattern for the pristine Cu_2O. (e) Representative SEM image of the pristine Cu_2O. (g) EPR spectra of the pristine, Ar-20, Ar-40 and Ar-60.

$((^{14}NH_4)_2SO_4$, 99.0%), sodium hydroxide (NaOH, 95.0%), polyethylene glycol (PEG-6000), ascorbic acid ($C_6H_8O_6$, 99.0%), sodium nitrate-^{15}N ($Na^{15}NO_3$, $^{15}N \geq 99$ at%, 98.5%), maleic acid ($C_4H_4O_4$, $\geq 99.0\%$), ammonium sulfate-^{15}N ($(^{15}NH_4)_2SO_4$, $^{15}N \geq 99$ at%, 98.5%), and dimethyl sulfoxide (DMSO, $\geq 99.9\%$) were purchased from Macklin. Sodium nitrate-^{14}N ($NaNO_3$, 99.0%) was purchased from Aladdin. Milli-Q water (18.25 MΩ cm^{-1}) was applied across the whole experiments.

2.2. Synthesis of pristine and plasma-treated Cu₂O

Cu_2O was synthesized by a liquid deposition method. 50 mL of polyethylene glycol (PEG-6000, ρ = 0.3 g L^{-1}) solution was mixed with 50 mL $CuSO_4$ (0.005 mol) solution under stirring for 30 min 100 mL of ascorbic acid (0.9 g) and NaOH (0.4 g) were added to the obtained Cu-containing solution with continuous stirring. After stirring for 7 h, the resultant mixture was centrifuged and dried at 60 ℃ for 6 h to form Cu_2O powders. The pristine Cu_2O was treated by Ar plasma for different time length ranging from 20 to 60 min. The plasma treatments were carried out in a vacuum chamber with an Ar pressure of 20 Pa, a Radio Frequency (RF) generator power of 200 W. Before plasma treatments, high purity argon gas was used to purge the vacuum chamber for 10 min to ensure that no other residual gas presented when plasma was excited. The samples subjected to plasma treatment for 20 min, 40 min and 60 min were labeled as Ar-20, Ar-40 and Ar-60 in the following context.

2.3. Materials characterization

X-ray Diffraction (XRD, Bruker D8 ADVANCE, Germany) was performed to determine the crystal structure of the samples. The morphologies and lattice structures were observed by Scanning Electron Microscope (SEM, SU-8010, Japan) and Transmission Electron Microscopy (TEM, Tecnai-G20, FEI). The surface chemistry was characterized by X-ray photoelectron spectroscopy (XPS, Esca lab 250Xi, Thermo Fisher Scientific, USA) with monochrome Al-Kα X-ray source. All the XPS Spectra were calibrated by using the C 1s peak at 284.6 eV. The synchrotron-based X-ray absorption spectra (XAS) were measured at the BL02B02 station of Shanghai Synchrotron Radiation Facility (SSRF). The concentration of oxygen vacancy was detected by Electron Paramagnetic Resonance (EPR, Bruker A300-10/12, Germany). The ultraviolet-visible (UV-Vis) absorbance spectra were measured on UV-1800 (Shimadzu, Japan) spectrophotometer.

2.4. Nitrate reduction reaction measurement

The electrochemical nitrate reduction reaction experiments were carried out using a standard three-electrode system in a H-type electrolytic cell separated with a Nafion membrane. The Cu_2O samples were mixed with deionized water, isopropyl alcohol and 5 wt% Nafion solution, and were then applied to the carbon paper substrate (2.06 cm^2). The obtained Cu_2O/CP electrode, saturated Ag/AgCl electrode and Pt-sheet were used as the working electrode, reference electrode, and counter electrode, respectively. 0.5 M sodium sulfate aqueous solution was used as the electrolyte, and a certain concentration of sodium nitrate was added to the cathode cell as the target reactant. All the electrochemical measurements were performed using CHI-660E electrochemical station (CH Instruments, China). All electrode potentials were given vs. the Ag/AgCl electrode. The linear sweep voltammetry (LSV) measurements were carried out with a scan rate of 5 mV s^{-1}. The electrochemical impedance spectroscopy (EIS) measurements were performed at − 1.1 V vs. the Ag/AgCl electrode for NO_3^-RR and HER with an amplitude of 5 mV and a frequency ranging from 10^6 to 10^{-2} Hz. The concentrations of NO_3^-, NO_2^- and NH_3 in the collected solution were quantified by ultraviolet-visible (UV-Vis) measurements (Supporting information; Fig. S1). The gas phase products were tested using gas chromatography (GC-9790II, FULI Instruments, China) equipped with flame ionization detector (FID) and thermal conductivity detector

(TCD). The detailed calculation formulas of selectivity, Faradaic efficiency and yield were shown in Supporting information.

2.5. N isotope labeling experiments

The N isotopic labeling experiments were carried out using the chronoamperometry methods (at −1.2 V vs. Ag/AgCl, for 6.0 h) in the electrolyte (200 ppm NO_3^--N) with $Na^{15}NO_3$ and $Na^{14}NO_3$ as N source, respectively. The amount of produced $^{15}NH_3$ and $^{14}NH_3$ was quantified by the 1H-Nuclear Magnetic Resonance (NMR) spectroscopy. For the NMR measurement, 30 μL collected electrolyte (with NH_3 products) was mixed with maleic acid (as the internal standard) aqueous solution (10 μL, 3.6 mM), H_2SO_4 aqueous solution (10 μL, 4 M), and DMSO (250 μL). Then, the obtained mixture was sealed into an NMR tube (600 MHz) for further tests. All 1H NMR tests were conducted with water-suppression using the pre-saturation experiment. The concentration of produced $^{15}NH_3$ can be determined by comparing the integral area (I) of the vinylic singlets for maleic acid (6.26 ppm, 2H) and the typical triplet for ammonium (7.18 ppm, 4H).

2.6. In-situ DRIFT measurement

The DRIFT measurements were performed on a Nicolet-6700 spectrometer (Thermo Scientific, America) equipped with a liquid-nitrogen-cooled HgCdTe (MCT/A) detector and an external reflection electrochemical accessory. The electrochemical tests during DRIFT measurement were carried out in a customized three-electrode electrochemical single-cell using CHI-660E electrochemical station. The catalyst (10 μg) supported by a glassy carbon electrode was used as the working electrode. A saturated Ag/AgCl and a Pt-wire were used as reference and counter electrode, respectively. The optical stage and CaF_2 prism were adjusted to appropriate angles to direct the incident infrared ray to the working electrode surface. The in-situ DRIFT/LSV measurement were carried out with a scan rate of 1 mV s^{-1} and applied potentials ranging from − 0.2 to − 1.4 V. For continuously collection of DRIFT spectra during NO_3^-RR, each spectrum was scanned 32 times with a spectral resolution of 4 cm^{-1} and a time interval of 0.2 min.

2.7. Computational method

The DFT calculations are performed by Vienna Ab initio Simulation Package (VASP) with the projector augmented wave (PAW) method. The exchange-functional is treated using the generalized gradient approximation (GGA) of Perdew-Burke-Ernzerhof (PBE) functional. The energy cutoff for the plane wave basis expansion was set to 450 eV. The force on each atom less than 0.02 eV/Å was set for convergence criterion of geometry relaxation. A 15 Å vacuum was added along the z direction in order to avoid the interaction between periodic structures. The Brillouin zone integration is performed using $3 \times 3 \times 1$ k-point sampling. The self-consistent calculations apply a convergence energy threshold of 10^{-4} eV. The DFT-D3 method was employed to consider the van der Waals interaction. To take into account the on-site Coulomb interaction between 3d electrons of Cu, the GGA+U approach was also employed with a U-J value of 4 eV proposed by Li et al. for Cu_2O system [27].

The free energies of the NO_3^- reduction reaction steps (NO_3^-RR) were calculated by the equation: $\Delta G = \Delta E_{DFT} + \Delta E_{ZPE} - T\Delta S$, where ΔE_{DFT} is the DFT electronic energy difference of each step, ΔE_{ZPE} and Δ_S are the correction of zero-point energy and the variation of entropy, respectively, which are obtained by vibration analysis, T is the temperature (T = 298 K).

3. Results and discussion

3.1. Characterization of the pristine and plasma-treated Cu₂O

The crystal structures of the samples before and after Ar plasma

treatment for 20 min, 40 min and 60 min, which were labeled as pristine, Ar-20, Ar-40 and Ar-60, were characterized by XRD measurements. As shown in the XRD patterns (Fig. 1b), the diffraction peaks of the pristine, Ar-20, Ar-40 and Ar-60 samples were well coincident with JCPDS no. 05-0667 for Cu_2O, suggesting that all the samples we obtained were Cu_2O with no other impurities such as Cu and CuO species [28]. We observed no obvious peak shifting and the disappearance/appearance of additional peaks for plasma-treated Cu_2O. The FWHM increased slightly after plasma treatment (Fig. S3a and b). This result implied that the plasma treatment did not introduce extra phased into the bulk structure of Cu_2O, but slightly decreased crystallinity of the material, which may be caused by the presence of surface oxygen vacancies. The interplanar spacing of the Cu_2O was calculated to be 0.246 nm and 0.213 nm, which matched the lattice parameters for the (1 1 1) and (2 0 0) plane for Cu_2O, respectively [29,30].

The SEM images (Fig. 1e) showed that the pristine Cu_2O nanoparticles were in spheroid shape with diameters of approximately 100–200 nm. The morphology remained unchanged after Ar plasma treatment (Fig. S2a). The detailed crystal structure of the pristine Cu_2O and the Ar-40 sample was probed by TEM technology, as shown in Fig. 1c-d and S2c-e. The HRTEM image of the pristine Cu_2O (Fig. 1d) showed that the spacing of characteristic lattice fringes were ∼ 0.246 nm and ∼ 0.213 nm, corresponding to the (1 1 1) and (2 0 0) of Cu_2O, respectively. Fig. 1f showed the diffraction pattern of pristine Cu_2O with clear diffraction rings of (1 1 1), (1 1 0) and (2 0 0). The TEM results of the Ar-40 (Fig. S2c–e) showed very similar characteristics as the pristine sample, implying that plasma treatment induced negligible changes in the bulk crystalline structure.

The electron paramagnetic resonance (EPR) test was performed to determine the oxygen vacancy concentration in the pristine and plasma-treated Cu_2O samples. As shown in the Fig. 1g, the characteristic peak at $g = 2.003$ is attributed to the formation of free electrons trapped by oxygen vacancies [22,31–33]. The intensity of EPR signal ($g = 2.003$) increased significantly with the prolongation of Ar plasma treatment time, indicating the increase of oxygen vacancy concentration with the treatment time. Considering the fact that both XRD and TEM showed no

noticeable difference between the pristine and plasma-treated Cu_2O samples, these oxygen defect generated by the plasma treatment are likely to be located in the near surface region.

To further reveal the impact of Ar plasma treatment on the surface properties of Cu_2O, XPS measurements were performed to determine the chemical environment of oxygen and copper for the pristine and plasma-treated Cu_2O samples. As shown in Fig. 2a, the O 1s XPS spectra were fitted into four components located at ∼ 530.1, ∼ 531.4, ∼ 532.5 and ∼ 534.0 eV, corresponding to lattice oxygen (lattice-O), defective oxygen (defective-O), surface hydroxyl group (hydroxyl-O) and adsorbed water molecules (H_2O), respectively [22,32,34]. The relative content of hydroxyl-O and defective-O were calculated by normalizing the area of corresponding peak to the total area of O 1s spectra, and the obtained results were shown in Fig. 2c. The defective-O content increased gradually with the prolongation of plasma treatment time, which was consistent essentially with the trend we observed in EPR spectra (Fig. 1g). The defective-O content decreased slightly when plasma treatment time increased to 60 min, which was likely due to the large amount of surface oxygen species formed on the surface. The contribution from surface hydroxyl-O for the Ar-20 and Ar-40 samples were significantly larger than that of the pristine (Fig. 2c), indicating that Ar plasma surface treatments enhanced hydroxylation of material surface. Such increase was attributed the formation of surface oxygen vacancies which effectively facilitate the formation of hydroxyl groups on the surface of metal oxides ($H_2O + V_o·· → 2OH^-$) [18,35]. However, due to the excessive etching and the dehydroxylation caused by exorbitant energy of plasma, further increase of the Ar plasma treatment time resulted in the loss of surface hydroxyl groups [25,36].

The Cu 2p spectra for the pristine and plasma-treated Cu_2O samples were fitted with three sets of spin-orbital splitting doublets (Fig. 2b), described as Cu^I-O, Cu^{II}-O, Cu^{II}-OH, and a satellite peak of Cu^{2+} [37,38]. The Cu^I-O doublet (orange peaks) located at the lowest binding energy represented the Cu species with oxidation state of one or zero [39,40]. Since we have not observed any metallic phase in our samples based on the XRD and HRTEM results, we assign this peak to Cu (I) in the Cu_2O lattice. While the Cu^{II}-O doublets (dark blue peaks) were attributed to
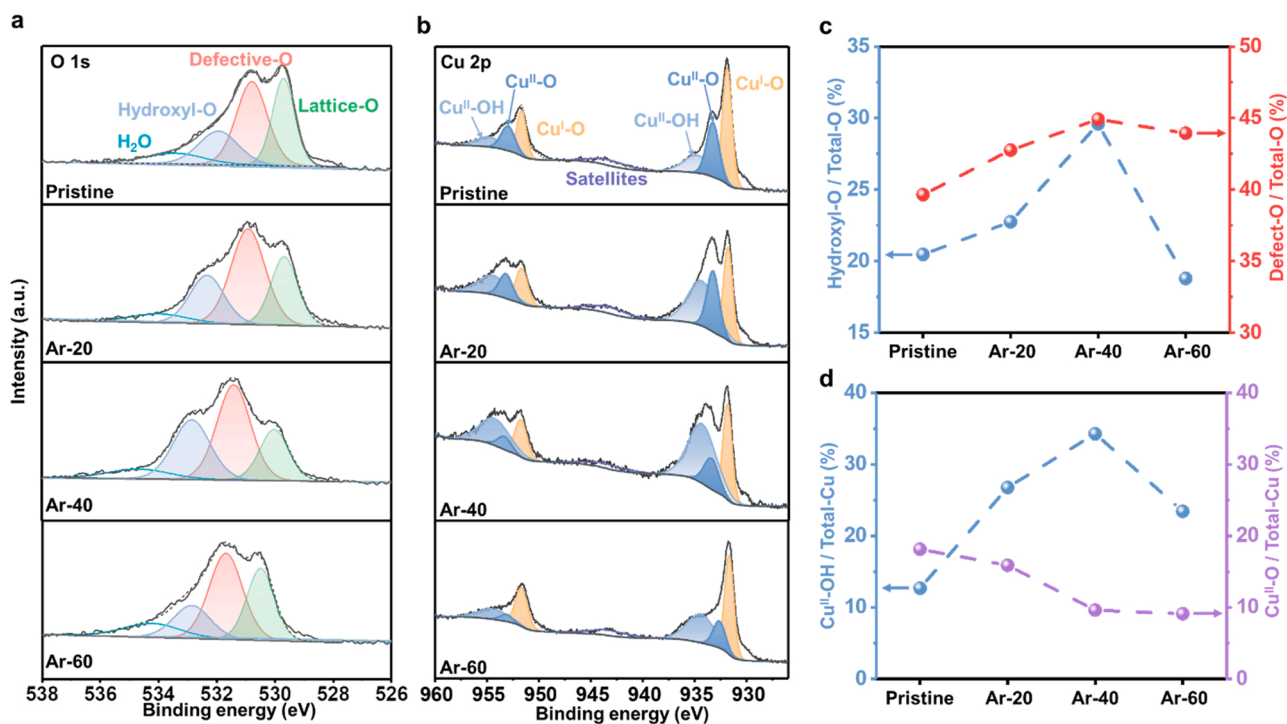

Fig. 2. (a) O 1s XPS spectra of pristine, Ar-20, Ar-40 and Ar-60. (b) Cu 2p XPS of pristine, Ar-20, Ar-40 and Ar-60. (c) Area percentage of O species for pristine, Ar-20, Ar-40 and Ar-60. (d) Area percentage of Cu species for pristine, Ar-20, Ar-40 and Ar-60.

the Cu (II) in copper oxides, the Cu^{II}-OH doublet (light blue peaks) located at the highest binding energy were assigned to Cu(II) bonding with hydroxyl groups [30,37,40]. The relative content of different copper species were calculated by normalizing the area of corresponding doublets to the total area of Cu 2p spectra, and the obtained results are shown in Fig. 2d. The Cu^{II}-OH species on the surface firstly increased with the plasma treatment time but showed a large decrease after 60 min treatment. Such volcano dependence of Cu^{II}-OH content with treatment time (Fig. 2d) is consistent with the trend we observed of the hydroxyl-O (Fig. 2c).

Both the O 1s and Cu 2p spectra consistently suggested that the surface hydroxylation was enhanced by short time plasma treatment (< 40 min), and a prolongate treatment time of 60 min led to a serious etching effect, which resulted in a decrease of hydroxyl groups on the surface. The Cu^{II}-O on the surface of the pristine sample were likely to form during the synthesis process and exposure to air [41,42]. The Cu^{II}-O content continuously decreased with plasma treatment, which was likely due to the formation of oxygen vacancies, resulting in the decrease of copper valence states.

To further obtain the information about the oxidization state of copper and the local density of states around the oxygen ligands, synchrotron-based soft XAS measurement with total-electron-yield (TEY) mode was performed for the pristine and the Ar-40 sample. To compare the spectra shape more clearly, the highest peak in the Cu L-edge spectra was normalized to be the same. As shown in Fig. 3a, two characteristic peaks located at ~ 934.7 and ~ 937.4 eV were observed on the Cu L-edge spectra, which were attributed to Cu (I) and Cu (II) [25,43]. The Cu (II) on the Ar-40 sample is noticeably higher than that of the pristine sample. The reason is likely that, although the Cu^{II}-O content in Ar-40 sample were lower than that on the pristine sample due to oxygen vacancy formation, the surface Cu^{II}-OH content was significantly higher. As a consequence, the total amount of Cu (II) species on Ar-40 samples was higher than that of the pristine Cu$_2$O. The increase of Cu (II) content in plasma-treated Cu$_2$O can be also confirmed by its higher intensity of Cu L-edge XAS spectra, which suggests a larger number of unoccupied density of states on Cu sites, as shown in the XAS spectra without intensity normalization in Fig. S3c.

The O K-edge spectra of Cu$_2$O and Ar-40 powders were shown in Fig. 3b. The peak located at ~ 533.4 eV was attributed to the hybridization of the O 2p with Cu 3d orbitals, while the broad peak located at ~ 539.9 eV was assigned to the O 2p/Cu 4sp states [44,45]. The intensity of O 2p/Cu 3d character showed a significantly drop after Ar plasma treatment, suggesting that the density of state (DOS) near oxygen ligand was noticeably higher after plasma treatment [46–48]. Such increase of DOS near oxygen ligand is likely correlated to the increase of Cu^{II}-OH group as observed in the Cu L edge XAS spectra (Fig. 3a) and XPS results (Fig. 2b). In addition, the obvious decreased intensity of O 2p/Cu 3d hybridized state (Fig. 3b, ~ 533.4 eV) for the Ar-40 relative to

that for the pristine sample indicated a weaker covalency and higher ionic M–O bonding in the material system [45,49]. Such change of surface oxygen environment may adjust the interaction between intermediate with catalyst, thus optimizing the reaction activity [11,50].

3.2. Electrochemical nitrate reduction activity

Having confirmed that plasma treatment effectively tuned oxygen vacancies and hydroxyl group on Cu$_2$O surfaces, we further evaluated the impact of plasma treatment on the NO$_3^-$RR performance of Cu$_2$O by using a typical three-electrode electrochemical system.

First, LSV measurements were carried for all the Cu$_2$O samples in 0.5 M Na$_2$SO$_4$ electrolyte with or without 200 ppm NO$_3^-$. As shown in LSV curves obtained in electrolytes without NO$_3^-$ (dash line in Fig. 4a), the current related to hydrogen evolution reaction (HER) is very small and only appears when the voltage is more negative than $- 1.4$ V, indicating the poor HER activity of our Cu$_2$O samples. Significantly higher current density was obtained in electrolyte containing NO$_3^-$ at the same potential (solid line in Fig. 4a), indicating that the current (under $- 0.8$ to $- 1.3$ V vs. Ag/AgCl) mainly came from NO$_3^-$RR and with negligible contribution from HER.

All the Cu$_2$O samples subjected to plasma treatment exhibited noticeable better NO$_3^-$RR performance in comparison to the pristine sample, as shown in the LSV curves of Fig. 4a. The current density for NO$_3^-$RR first increase (pristine → Ar-40) and then decrease (Ar-60) with increasing Ar plasma treatment time. The Ar-40 showed highest current density at different potentials from $- 0.8$ to $- 1.3$ V vs. Ag/AgCl. The EIS spectra of all the samples are dominated by a semicircle (Fig. S5), which can be fitted by a system ohmic resistance (R$_\Omega$), a charge transfer resistance (R$_{ct}$) and a constant capacitive element (C$_D$) of the electrochemical testing environment [51]. Under the same test system, all the samples exhibited very similar R$_\Omega$, which was used for ohmic compensation of LSV. The fitting results of different samples followed a consistent trend with the LSV results. The R$_{ct}$ value of plasma treated Cu$_2$O was much smaller than that of pristine Cu$_2$O, representing more favorable reaction process for the plasma treated samples. The Ar-40 exhibited the lowest charge transfer resistance (10.57 Ω) and most favorable reaction kinetics across the solid/liquid interface of nitrate system [52].

The NH$_3$ selectivity and NO$_3^-$ conversion of different samples were further studied in 0.5 M Na$_2$SO$_4$ with 200 ppm nitrate, and the reaction products were measured after holding the reaction at a certain potential for 6.0 h. As shown in Fig. 4b and c, the NO$_3$ conversion rate, NH$_3$ selectivity, Faradaic efficiency and NH$_3$ yield rate show a volcanic dependence on plasma treatment time, which match with the LSV and EIS measurement results. While all the plasma-treated sample exhibited better performance than the pristine one, the Ar-40 sample displayed the highest NH$_3$ selectivity (85.78%), NO$_3^-$ conversion (95.11%), Faradaic
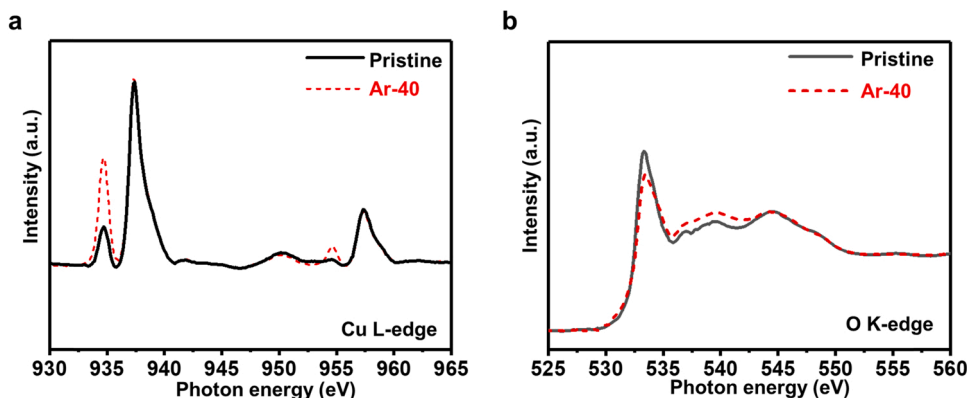

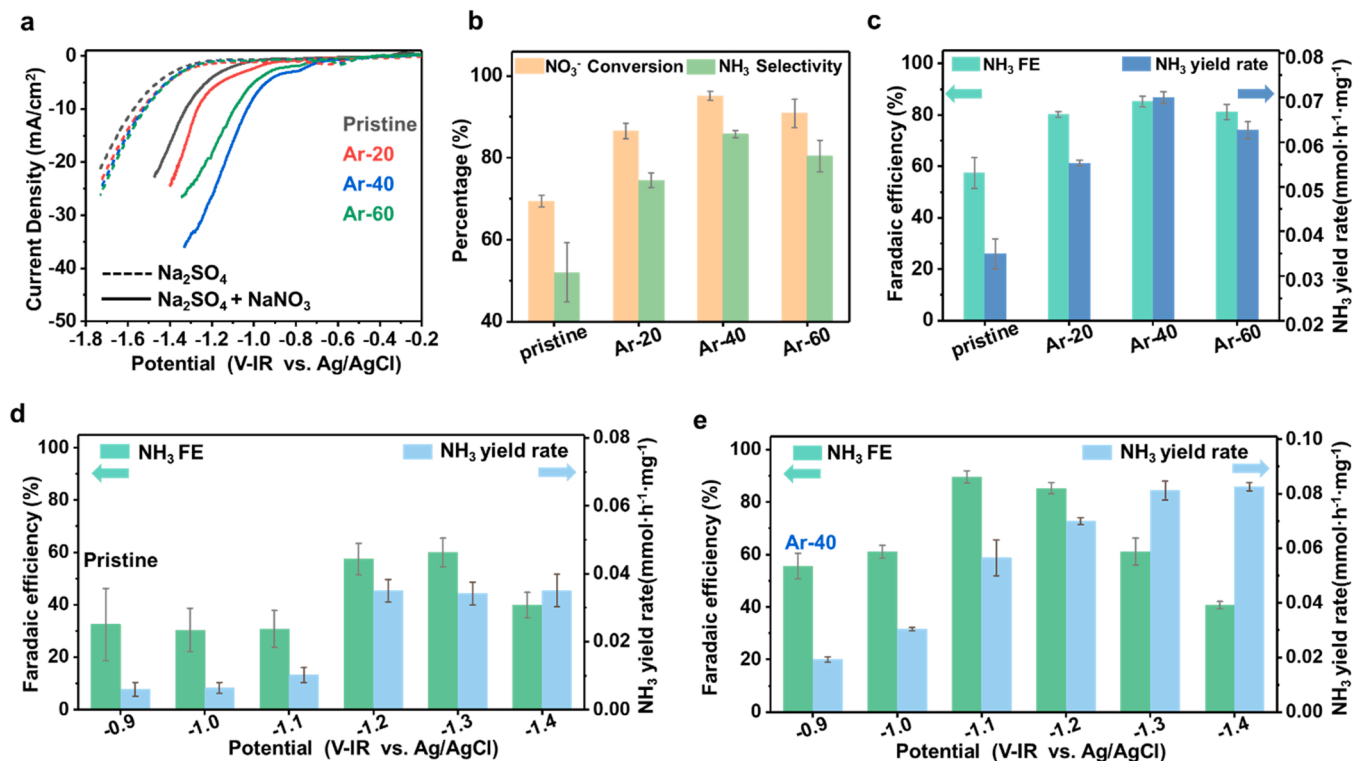**Fig. 3.** (a) Cu L-edge XAS spectra of pristine and Ar-40. (b) O K-edge XAS spectra of pristine and Ar-40.

Fig. 4. (a) LSV curves with IR-compensation for the pristine, Ar-20, Ar-40 and Ar-60 in 0.5 M Na$_2$SO$_4$ electrolyte with or without 200 ppm nitrate. (b) The nitrate conversion and ammonia selectivity of pristine, Ar-20, Ar-40 and Ar-60 at − 1.2 V vs. Ag/AgCl. (c) The Faradaic efficiency and yield rate of ammonia formation catalyzed by pristine, Ar-20, Ar-40 and Ar-60 with 50 ppm N-NO$_3^-$ at − 1.2 V vs. Ag/AgCl for 6 h. (d–e) The comparisons of ammonia Faradaic efficiency and yield rate between the pristine and Ar-40 sample with 50 ppm N-NO$_3^-$ at different potential. The error bar of each data point represents the experimental uncertainties.

efficiency (85.26%) and NH$_3$ yield rate (0.0699 mmol h^{-1} mg^{-1}) for ammonia production at − 1.2 V with 30 mA/cm^2 (Fig. 4b and c).

To further confirm the improved NO$_3^-$RR performance by plasma treatment, we compared the reaction products of the constant-potential electrolysis under different potentials for the pristine samples (Fig. 4d) and Ar-40 sample (Fig. 4e). For both samples, the Faradaic efficiency of NH$_3$ formation firstly increase with applied potential and then decreased. The decrease of Faradaic efficiency at high applied potential is due to the higher contribution of hydrogen evolution current (Gas phase products H$_2$ testing by gas chromatography, Fig. S8). This is because the protons required for NO$_3^-$RR in neutral solution are usually provided by H$_2$O. When a too high negative potential was applied to the electrode, it is unfavorable for the adsorption of nitrate, resulting in more favorable kinetic processes of HER, thereby reducing ammonia

Faradaic efficiency [53]. For the pristine sample, the Faradaic efficiency of NH$_3$ formation ranged from ~ 32.43% to ~ 57.47% with the potential from − 0.9 V to − 1.2 V vs. Ag/AgCl. In contrast, the Faradaic efficiency for the Ar-40 sample ranged from 55.59% to 89.54% under the sample potential range. The highest Faradaic efficiency for the Ar-40 sample was 89.54% at − 1.1 V vs. Ag/AgCl (Fig. 4e), which was much larger than the highest Faradaic efficiency for the pristine sample at 60.01% at − 1.2 V vs. Ag/AgCl. The NH$_3$ yield rates were found to increase with the applied potential and reached a nearly stable value for both the pristine sample and the Ar-40 samples. The stable NH$_3$ yield rate of Ar-40 (0.0825 mmol h^{-1} mg^{-1}) was significantly higher than that of pristine sample (0.0351 mmol h^{-1} mg^{-1}). The impacts of nitrate concentration, reaction time and cycling test on the NO$_3^-$RR performance were further discussed in Supporting information (Figs. S9–S11).
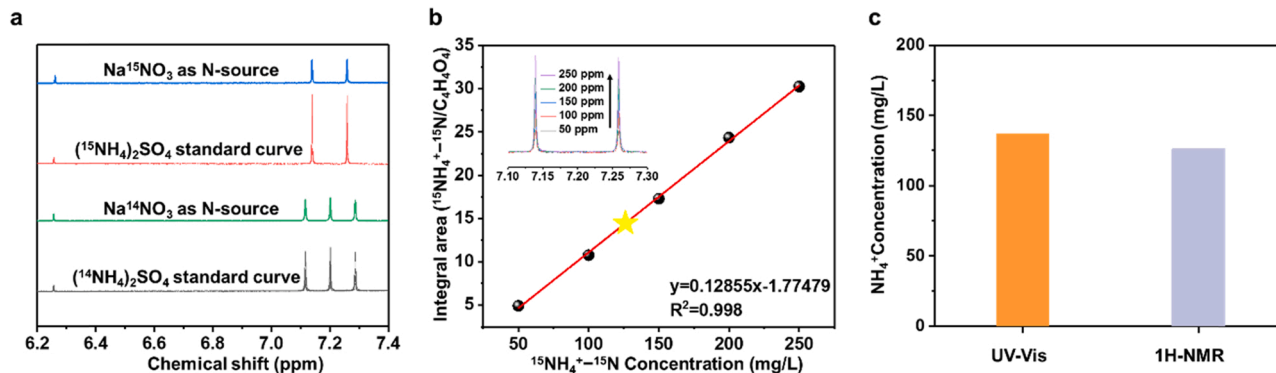

Fig. 5. (a) 1H NMR tests of produced ammonia using Na^{14}NO$_3$ and Na^{15}NO$_3$ as nitrogen sources. (b) The standard curve of integral area (^{15}NH$_4^+$–^{15}N/C$_4$H$_4$O$_4$) against ^{15}NH$_4^+$–^{15}N concentration. The inset figure shows the 1H NMR spectra of ^{15}NH$_4^+$–^{15}N with different concentration. The star marked the ^{15}NH$_4^+$–^{15}N concentration quantified for our experiment. (c) The quantification of ammonia via UV-Vis and 1H NMR measurements.

In addition, ^{15}N isotope labeling experiments were carried out to verify the sources of NH₃. We carried out chronoamperometry measurement at − 1.2 V vs. Ag/AgCl for 6.0 h in the electrolyte with Na[15]NO₃ and Na[14]NO₃ as N source, respectively. As shown in Fig. 5a, when the electrolysis was carried out in solution with Na[14]NO₃, the 1H NMR (600 MHz) spectra of obtained products showed typical triple peaks of [14]NH₄⁺. In contrast, when the Na[15]NO₃ was used as nitrogen source, the 1H NMR (600 MHz) spectra of obtained products showed typical double peaks of [15]NH₄⁺ [54,55]. Such results indicated that the produced ammonium was entirely derived from the nitrate in the electrolyte, rather than from the reaction setup, electrode material and air. Maleic acid ($C_4H_4O_4$) was employed as an internal standard for quantifying the produced NH₃. The standard curve of the integral area (NH₄⁺-^{15}N/$C_4H_4O_4$) against NH₄⁺-^{15}N concentration was established to determine the concentration of NH₄⁺-[15]N (Fig. 5b). As shown in Fig. 5c, the concentration of NH₄⁺-^{15}N detected via 1H NMR is very close to that from UV-Vis. These results suggest that all the ammonia products are produced from the nitrate in the solution, and the Nessler's reagent colorimetric method is a reliable method for determining ammonia products.

All the electrochemical results suggested that the plasma treatment effectively promote the NO₃⁻RR activity of Cu₂O. The NO₃⁻RR activity of Cu₂O showed a volcano-type dependence on the plasma treatment time, with the Ar-40 sample to show the highest activity. Such dependence of activity on the plasma treatment time is consistent with what we observed for the surface hydroxyl-O groups, which firstly increased with Ar plasma time due to the facilitated surface hydroxylation process, and then decreased due to the etching effect. The Ar-40 exhibited the highest NO₃⁻RR performance as well as the largest amount of hydroxyl group on the surface. As will be shown in the latter section, we believe that, while the oxygen vacancy facilitates the adsorption of nitrate species, the hydroxyl group promote the proton-transfer steps in the reaction. Both effects lead to the enhanced NO₃⁻RR activity of the plasma-treated Cu₂O.

3.3. Elucidation of the NO₃⁻RR mechanism

To explore the mechanism for the enhanced NO₃⁻RR activity of

plasma-treated Cu₂O, In-situ DRIFT was carried out to identify adsorbed intermediates on the surface of Cu₂O during the reaction. The nitrate reduction reactions on electrocatalysts surface are reported as the follows [7,56]:
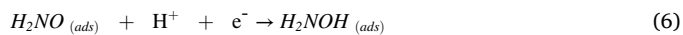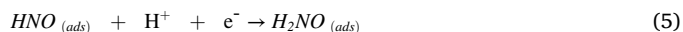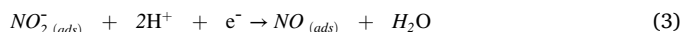
$$NO_3^- \quad \rightarrow \quad NO_3^-(ads) \tag{1}$$

$$NO_3^-(ads) + 2H^+ \;+\; 2e^- \rightarrow \; NO_2^- \;+\; H_2O \tag{2}$$

$$NO_{2\,(ads)}^- \;+\; 2H^+ \;+\; e^- \rightarrow NO_{(ads)} \;+\; H_2O \tag{3}$$

$$NO_{(ads)} \;+\; H^+ \;+\; e^- \rightarrow HNO_{(ads)} \tag{4}$$

$$HNO_{(ads)} \;+\; H^+ \;+\; e^- \rightarrow H_2NO_{(ads)} \tag{5}$$

$$H_2NO_{(ads)} \;+\; H^+ \;+\; e^- \rightarrow H_2NOH_{(ads)} \tag{6}$$

$$H_2NOH_{(ads)} \;+\; 2H^+ \;+\; 2e^- \rightarrow NH_3 + H_2O \tag{7}$$

Fig. 6 shows the DRIFT spectra obtained from the NO₃⁻RR in the solution containing 200 ppm NO₃⁻. As shown in the In-situ DRIFT spectra obtained during the LSV measurements in nitrate solution (Fig. 6a and c), characteristic peaks at about ∼ 1300 cm⁻¹ (peak 1) appeared at low applied potential, which are corresponding to the pre-coordination nitrate species (*NO₃⁻) got absorbed on the surface (*formula (1)*) [57]. As the applied potential increased, the nitrate species (peak 1) gradually reduced, and two characteristic peaks at ∼ 1200 and ∼ 1250 cm⁻¹ (peak 2) showed up, which are assigned to the bidentate coordination between metal and nitrate or nitrite species (*-O₂N) [58]. Such appearance of bidentate coordination was attributed to the adsorption and coordination of nitrite, which need to undergo a two proton/electron transfer nitrate reduction process and release a water molecule (*formula (2)*). As the applied potential further increased, the bidentate coordination of nitrate or nitrite was gradually transformed to the monodentate coordination of *N-O species (peak 3, *formula (3)*).

Although the In-situ DRIFT spectra of the pristine and Ar-40 samples appeared to evolve similarly with applied potential, the appearance of the new formed peaks (especially bidentate nitrite and monodentate
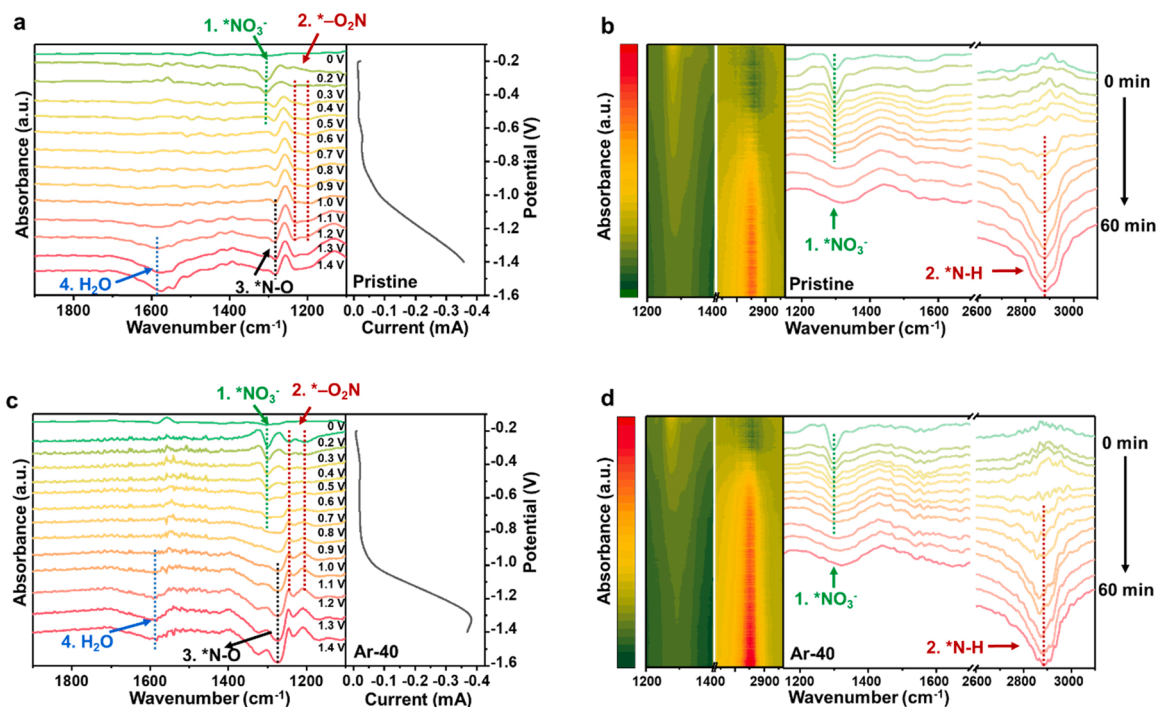

Fig. 6. In-situ DRIFT spectra of nitrate electroreduction on (a) pristine and (c) Ar-40 as a function of potential. Time-dependent of In-situ DRIFT spectra obtained during chronoamperometry measurement at an applied potential of at − 1.2 V vs. Ag/AgCl in nitrate solution as a function of time for (b) pristine and (d) Ar-40.

coordination of *N-O, peak 2 and 3) occurred at noticeably lower applied potential and with much higher intensity (Fig. 6a and c). This result implied that Ar-40 exhibited stronger adsorption for above species and higher catalytic activity for catalyzing the above steps to occur (*formulas* (2) and (3)). The absorption peaks located at ~ 1600 cm (Peak 4), which are corresponding to the bending vibration of adsorbed water molecules, were noticeable higher on the pristine sample in comparison to the Ar-40 samples. Such accumulation of water molecules on the pristine sample was likely due to its slow rate of water dissociation and proton supply.

Fig. 6b and d presented the in-situ DRIFT spectra obtained during chronoamperometry measurement at an applied potential of − 1.2 V in nitrate solution as a function of time. Similar to the spectra obtained during LSV measurement, the accumulation of nitrate (peak 1, 1300 cm^{-1}, *NO$_3^-$) was observed at the initial time of electrolysis on both samples. As the electrolysis time elongated, the peak of nitrate (peak 1) continued to decrease, suggesting the consumption of the accumulated nitrate species. In the meantime, a strong and broad band appeared at 2800–3000 cm^{-1} region (peak 2, *N-H), which is attributed to the N-H asymmetric stretching vibration of *NH$_3$, implying the generation of ammonia as the final products. The transformation of nitrate species to ammonia species can be observed directly by the mapping of in-situ DRIFT spectra. Although it is difficult to detect the evolution of intermediate species due to the limitation of time-resolution, a significantly higher concentration of ammonia was observed on the Ar-40 samples in comparison to the pristine one. This result provided direct evidence for the higher electrocatalytic activity for the plasma-treated Cu$_2$O samples than the pristine one. The detailed assignment of IR bands appearing during the nitrate reduction process is shown in Table S1.

Our in-situ DRIFT measurement provided consistent results about the reaction steps of NO$_3^-$RR reported in literature (*formulas* (1)–(7), Fig. 6). The nitrate firstly got absorbed on the surface and then is transformed into nitrite through a proton and electron transfer process (*formulas* (1)–(2)). The adsorbed nitrite species or bidentate nitrite were further reduced to *N-O (*formulas* (3)–(4)). Subsequently, a series of hydrogenation processes on the Cu-*N-O site (*NO→*ONH→*ONH$_2$→*ONH$_3$, *formulas* (4)–(7)) occurs, and lead to the final formation of ammonia [59,60].

To understand the impact of oxygen vacancy on the NO$_3^-$RR activity, we carried out DFT calculation to determine the local charge density around the Cu site before and after oxygen vacancy formation. According to Bader charge analysis (Fig. 7a and b), the polarization charge density of Cu around oxygen vacancy (10.78 e$^-$) is noticeable higher than that of Cu in the pristine sample (10.46 e$^-$). In the meantime, the valence state of Cu decreased after oxygen vacancy formation. These results suggested that the extra electron generated during oxygen vacancy formation got localized near the Cu site. Consistently with such changes in local charge density, the state corresponding to Cu d-orbital shifted closed to the Fermi level, as shown in the partial density of states (PDOS) in Fig. S13. The higher charge density near the Cu sites and the upshifted d-orbital may promote the electron transfer between the surface and reaction intermediates [21,61,62], leading to strongly improved NO$_3^-$RR.

To further reveal the reaction mechanism, the energetics of reaction pathways for NO$_3^-$RR were determine by DFT calculation. As shown in Fig. 7c, the adsorption energy of NO$_3^-$ on Cu$_2$O (111) with one oxygen vacancy (Cu$_2$O with OV) is − 2.25 eV, which is significantly lower than that on the pristine Cu$_2$O (111) surface (− 0.97 eV). Such result is
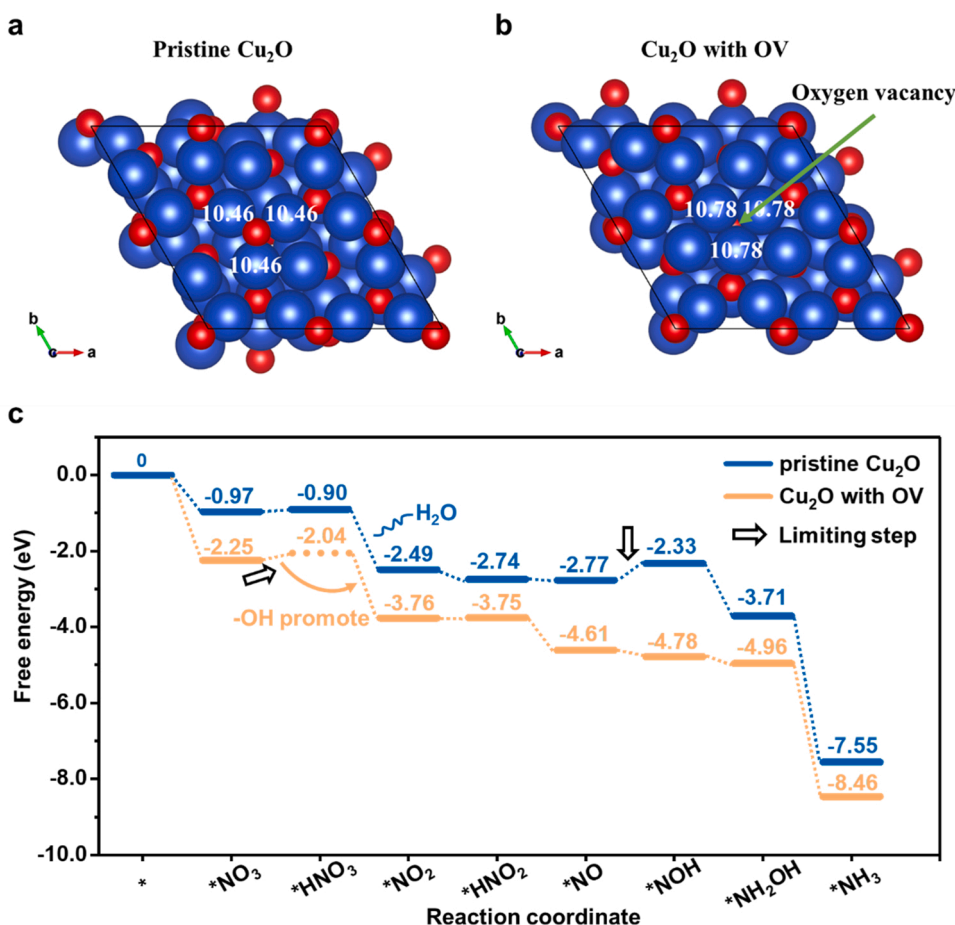

Fig. 7. The polarization charge density before (a) and after (b) oxygen vacancy formation obtained by Bader charge analysis. (c) The energetics of reaction pathways by theoretical calculation for different intermediates on Cu$_2$O (111).

consistent with the strongly enhanced NO_3^- adsorption on the Ar-40 surface as we observed by In-situ DRIFT measurement. Similar lower adsorption energy was also found for other reaction intermediation on Cu_2O with OV in comparison to that on the pristine surface (Fig. 7c).

For the pristine Cu_2O sample, the hydrogenation of $*NO_3$ to $*HNO_3$ ($*NO_3 \rightarrow *HNO_3$) and $*NO$ reduction to $*NOH$ ($*NO \rightarrow *NOH$) are two key steps that are required to overcome certain energy barriers (Fig. 7c). Similarly, the hydrogenation of $*NO_3$ ($*NO_3 \rightarrow *HNO_3$) and $*NO_2$ ($*NO_2 \rightarrow *HNO_2$) on Cu_2O with OV also are required to overcome energy barriers to occur. These results implied the critical role of hydrogenation reaction steps during NO_3^-RR, which is in agreement with previous calculation results reported on other transition metal-based materials [13,15,63].

The reaction barrier for the rate limiting step (RLS) of NO_3^-RR on the pristine Cu_2O (111) ($*NO \rightarrow *NOH$) is 0.44 eV, which is noticeably higher than the RLS step on the Cu_2O with OV ($*NO_3 \rightarrow *HNO_3$). Such a reduced reaction barrier for the RLS step on defective Cu_2O surface is likely be one reason for its higher ammonia selectivity as we observed experimentally (Fig. 4) [7,64].

As shown in previous section, the plasma treated Cu_2O not only presented higher oxygen vacancy concentration but also richer surface hydroxyl group. Guo et al. [65] reported that a H bonded to the O site next to the Cu active site could evolve to a state in which H was bonded to the O in the $*NO_3$ group. Such state is actually similar with the configuration of $*HNO_3$ intermediates got absorbed on the Cu_2O surface during the reaction (Figs. S14 and S15). Therefore, we believe that the hydroxyl group on the copper oxide surface may promote proton transfer and the transformation of configuration for the RLS ($*NO_3 \rightarrow *HNO_3$) on the surface of Cu_2O with OV (Fig. 7c). The promotion effect of hydroxyl group can explain previous experimental results (Fig. 4), which showed that the catalytic activity of Ar-40 samples was better than that of the Ar-60 with higher oxygen vacancy concentration but lower surface hydroxyl density.

As revealed by the in-situ DRIFT results and DFT calculation from previous section, the adsorption and conversion of reaction intermediates on the Cu_2O surface is strongly modulated by plasma treatment. Such modulation was attributed to the impact of surface oxygen vacancies on local electronic structure. In addition, the conversation from nitrate to nitrite and $*N-O$ occurred was found to be more easily on the plasma treated surface (Fig. 6a and c). Protons was actively involved in these two reaction steps. Under neutral solution conditions, the cleavage of H–OH bond is the premise of providing protons [67,68]. The plasma treated sample exhibited better water dissociation and proton transfer, which is likely due to the presence of surface oxygen vacancies and hydroxyl [59,69], as revealed by the water peaks in Fig. 6a and c. We believe that the presence of surface oxygen vacancies and hydroxyl groups in combine promote the water dissociation and proton transfer process. [63,66].

4. Conclusion

In summary, we synthesized Cu_2O model system by a liquid deposition method and treated the obtained Cu_2O by Ar plasma for various time length. The SEM, TEM and XRD results confirmed that the morphology and bulk structure of Cu_2O showed negligible changes after Ar plasma treatment. The combination of XPS and synchrotron-based XAS measurements suggested that plasma treatment promoted the formation of oxygen vacancies and hydroxyl groups on the surface. Accompanied with such change in oxygen environment, the plasma-treated Cu_2O exhibited significantly improvement in activity and Faradaic efficiency for nitrate electroreduction to valuable ammonia. The Cu_2O subjected to 40 min plasma treatment exhibited the optimal NO_3^-RR activity, with the selectivity and Faradaic efficiency of ammonia reaching 85.7% and 89.54%, respectively. The ^{15}N isotope labeling experiments confirmed that the ammonia products entirely came from the nitrate electroreduction. The combination of surface analysis,

electrochemical measurement, in-situ DRIFT and DFT calculation results suggested that Ar plasma effectively tuned the surface oxygen species, facilitated the adsorption of nitrate as well as promote the proton transfer process, leading to the strongly enhanced NO_3^-RR activity. This study provides critical insight into the role of surface oxygen species in determining the nitrate reduction reaction activity. The mechanistic understanding obtained here can guide the use of surface engineering strategy for synthesizing high activity electrocatalyst in green energy and environment field.

CRediT authorship contribution statement

Zhiheng Gong: Conceptualization, Investigation, Formal analysis, Data curation, Methodology, Writing – original draft, Writing – review & editing. **Wenye Zhong:** Investigation, Data curation, Formal analysis, Validation. **Zuyun He:** Methodology, Investigation. **Qiuyu Liu:** Methodology, Investigation. **Haijun Chen:** Methodology. **Deng Zhou:** Methodology, Investigation. **Nian Zhang:** Resources. **Xiongwu Kang:** Resources. **Yan Chen:** Conceptualization, Funding acquisition, Project administration, Resources, Validation, Writing – review & editing.

Declaration of Competing Interest

The authors declare that they have no known competing financial interests or personal relationships that could have appeared to influence the work reported in this paper.

Appendix A. Supporting information

Supplementary data associated with this article can be found in the online version at doi:10.1016/j.apcatb.2021.121021.

References

[1] J.G. Chen, R.M. Crooks, L.C. Seefeldt, K.L. Bren, R.M. Bullock, M.Y. Darensbourg, P.L. Holland, B. Hoffman, M.J. Janik, A.K. Jones, M.G. Kanatzidis, P. King, K. M. Lancaster, S.V. Lymar, P. Pfromm, W.F. Schneider, R.R. Schrock, Beyond fossil fuel-driven nitrogen transformations, Science 360 (2018) eaar6611.

[2] K. Chu, Y.-p. Liu, Y.-b. Li, Y.-l. Guo, Y. Tian, H. Zhang, Multi-functional Mo-doping in MnO_2 nanoflowers toward efficient and robust electrocatalytic nitrogen fixation, Appl. Catal. B 264 (2020), 118525.

[3] Y. Zeng, C. Priest, G. Wang, G. Wu, Restoring the nitrogen cycle by electrochemical reduction of nitrate: progress and prospects, Small Methods 4 (2020), 2000672.

[4] M. Duca, M.T.M. Koper, Powering denitrification: the perspectives of electrocatalytic nitrate reduction, Energy Environ. Sci. 5 (2012) 9726.

[5] J. Martínez, A. Ortiz, I. Ortiz, State-of-the-art and perspectives of the catalytic and electrocatalytic reduction of aqueous nitrates, Appl. Catal. B 207 (2017) 42–59.

[6] L. Li, C. Tang, X. Cui, Y. Zheng, X. Wang, H. Xu, S. Zhang, T. Shao, K. Davey, S. Z. Qiao, Efficient nitrogen fixation to ammonia through integration of plasma oxidation with electrocatalytic reduction, Angew. Chem. Int. Ed. 133 (2021) 14250–14256.

[7] X. Zhang, Y. Wang, C. Liu, Y. Yu, S. Lu, B. Zhang, Recent advances in non-noble metal electrocatalysts for nitrate reduction, Chem. Eng. J. 403 (2021), 126269.

[8] G.-F. Chen, Y. Yuan, H. Jiang, S.-Y. Ren, L.-X. Ding, L. Ma, T. Wu, J. Lu, H. Wang, Electrochemical reduction of nitrate to ammonia via direct eight-electron transfer using a copper–molecular solid catalyst, Nat. Energy 5 (2020) 605–613.

[9] Y. Wang, Y. Yu, R. Jia, C. Zhang, B. Zhang, Electrochemical synthesis of nitric acid from air and ammonia through waste utilization, Natl. Sci. Rev. 6 (2019) 730–738.

[10] Y. Wang, W. Zhou, R. Jia, Y. Yu, B. Zhang, Unveiling the activity origin of a copper-based electrocatalyst for selective nitrate reduction to ammonia, Angew. Chem. Int. Ed. 59 (2020) 5350–5354.

[11] R. Jia, Y. Wang, C. Wang, Y. Ling, Y. Yu, B. Zhang, Boosting selective nitrate electroreduction to ammonium by constructing oxygen vacancies in TiO$_2$, ACS Catal. 10 (2020) 3533–3540.

[12] Y. Wang, C. Wang, M. Li, Y. Yu, B. Zhang, Nitrate electroreduction: mechanism insight, in situ characterization, performance evaluation, and challenges, Chem. Soc. Rev. 50 (2021) 6720–6733.

[13] Z.Y. Wu, M. Karamad, X. Yong, Q. Huang, D.A. Cullen, P. Zhu, C. Xia, Q. Xiao, M. Shakouri, F.Y. Chen, J.Y.T. Kim, Y. Xia, K. Heck, Y. Hu, M.S. Wong, Q. Li, I. Gates, S. Siahrostami, H. Wang, Electrochemical ammonia synthesis via nitrate reduction on Fe single atom catalyst, Nat. Commun. 12 (2021) 2870.

[14] J. Li, M. Li, N. An, S. Zhang, Q. Song, Y. Yang, X. Liu, Atomically dispersed Fe atoms anchored on S and N-codoped carbon for efficient electrochemical denitrification, Proc. Natl. Acad. Sci. USA 118 (2021), e2105628118.

[15] Q. Hu, Y. Qin, X. Wang, Z. Wang, X. Huang, H. Zheng, K. Gao, H. Yang, P. Zhang, M. Shao, C. He, Reaction intermediate-mediated electrocatalyst synthesis favors specified facet and defect exposure for efficient nitrate–ammonia conversion, Energy Environ. Sci. 14 (2021) 4989–4997.

[16] Q. Dang, S. Tang, T. Liu, X. Li, X. Wang, W. Zhong, Y. Luo, J. Jiang, Regulating electronic spin moments of single-atom catalyst sites via single-atom promoter tuning on S-vacancy MoS$_2$ for efficient nitrogen fixation, J. Phys. Chem. Lett. 12 (2021) 8355–8362.

[17] K. Chu, Y.-p. Liu, Y.-h. Cheng, Q.-q. Li, Synergistic boron-dopants and boron-induced oxygen vacancies in MnO$_2$ nanosheets to promote electrocatalytic nitrogen reduction, J. Mater. Chem. A 8 (2020) 5200–5208.

[18] Y. Zhu, Z. He, Y. Choi, H. Chen, X. Li, B. Zhao, Y. Yu, H. Zhang, K.A. Stoerzinger, Z. Feng, Y. Chen, M. Liu, Tuning proton-coupled electron transfer by crystal orientation for efficient water oxidization on double perovskite oxides, Nat. Commun. 11 (2020) 4299.

[19] A. Grimaud, O. Diaz-Morales, B. Han, W.T. Hong, Y.L. Lee, L. Giordano, K. A. Stoerzinger, M.T.M. Koper, Y. Shao-Horn, Activating lattice oxygen redox reactions in metal oxides to catalyse oxygen evolution, Nat. Chem. 9 (2017) 457–465.

[20] J. Hwang, R.R. Rao, L. Giordano, K. Akkiraju, X.R. Wang, E.J. Crumlin, H. Bluhm, Y. Shao-Horn, Regulating oxygen activity of perovskites to promote NO$_x$ oxidation and reduction kinetics, Nat. Catal. 4 (2021) 663–673.

[21] R. Huang, Y. Zhu, M.T. Curnan, Y. Zhang, J.W. Han, Y. Chen, S. Huang, Z. Lin, Tuning reaction pathways of peroxymonosulfate-based advanced oxidation process via defect engineering, Cell Rep. Phys. Sci. 2 (2021), 100550.

[22] Y. Zhu, L. Zhang, B. Zhao, H. Chen, X. Liu, R. Zhao, X. Wang, J. Liu, Y. Chen, M. Liu, Improving the activity for oxygen evolution reaction by tailoring oxygen defects in double perovskite oxides, Adv. Funct. Mater. 29 (2019), 1901783.

[23] Z. Xiao, Y.C. Huang, C.L. Dong, C. Xie, Z. Liu, S. Du, W. Chen, D. Yan, L. Tao, Z. Shu, G. Zhang, H. Duan, Y. Wang, Y. Zou, R. Chen, S. Wang, Operando identification of the dynamic behavior of oxygen vacancy-rich Co$_3$O$_4$ for oxygen evolution reaction, J. Am. Chem. Soc. 142 (2020) 12087–12095.

[24] Z. Gu, N. Yang, P. Han, M. Kuang, B. Mei, Z. Jiang, J. Zhong, L. Li, G. Zheng, Oxygen vacancy tuning toward efficient electrocatalytic CO$_2$ reduction to C$_2$H$_4$, Small Methods 3 (2019), 1800449.

[25] H. Mistry, A.S. Varela, C.S. Bonifacio, I. Zegkinoglou, I. Sinev, Y.W. Choi, K. Kisslinger, E.A. Stach, J.C. Yang, P. Strasser, B.R. Cuenya, Highly selective plasma-activated copper catalysts for carbon dioxide reduction to ethylene, Nat. Commun. 7 (2016) 12123.

[26] D. Gao, I. Zegkinoglou, N.J. Divins, F. Scholten, I. Sinev, P. Grosse, B. Roldan Cuenya, Plasma-activated copper nanocube catalysts for efficient carbon dioxide electroreduction to hydrocarbons and alcohols, ACS Nano 11 (2017) 4825–4831.

[27] L. Li, R. Zhang, J. Vinson, E.L. Shirley, J.P. Greeley, J.R. Guest, M.K.Y. Chan, Imaging catalytic activation of CO$_2$ on Cu$_2$O (110): a first-principles study, Chem. Mater. 30 (2018) 1912–1923.

[28] Y. Liu, H. Bai, Q. Zhang, Y. Bai, X. Pang, F. Wang, Y. Yang, J. Ding, W. Fan, W. Shi, In-situ decoration of unsaturated Cu sites on Cu$_2$O photocathode for boosting nitrogen reduction reaction, Chem. Eng. J. 413 (2021), 127453.

[29] Y. Liu, J. Lu, Q. Zhang, Y. Bai, X. Pang, S. Wang, H. Bai, W. Fan, Charge-transfer dynamics at a Ag/Ni-MOF/Cu$_2$O heterostructure in photoelectrochemical NH$_3$ production, Chem. Commun. 57 (2021) 8031–8034.

[30] Y.A. Wu, I. McNulty, C. Liu, K.C. Lau, Q. Liu, A.P. Paulikas, C.-J. Sun, Z. Cai, J. R. Guest, Y. Ren, V. Stamenkovic, L.A. Curtiss, Y. Liu, T. Rajh, Facet-dependent active sites of a single Cu$_2$O particle photocatalyst for CO$_2$ reduction to methanol, Nat. Energy 4 (2019) 957–968.

[31] C. Wang, L.-L. Gu, S.-Y. Qiu, J. Gao, Y.-C. Zhang, K.-X. Wang, J.-J. Zou, P.-J. Zuo, X.-D. Zhu, Modulating CoFe$_2$O$_4$ nanocube with oxygen vacancy and carbon wrapper towards enhanced electrocatalytic nitrogen reduction to ammonia, Appl. Catal. B 297 (2021) 120452.

[32] Q. Liu, Y. Zhu, Z. He, S. Jin, Y. Chen, A facile top-down approach for constructing perovskite oxide nanostructure with abundant oxygen defects as highly efficient water oxidation electrocatalyst, Int. J. Hydrog. Energy 45 (2020) 22808–22816.

[33] Y. Zhu, X. Zhong, S. Jin, H. Chen, Z. He, Q. Liu, Y. Chen, Oxygen defect engineering in double perovskite oxides for effective water oxidation, J. Mater. Chem. A 8 (2020) 10957–10965.

[34] Y. Pan, X. Xu, Y. Zhong, L. Ge, Y. Chen, J.M. Veder, D. Guan, R. O'Hayre, M. Li, G. Wang, H. Wang, W. Zhou, Z. Shao, Direct evidence of boosted oxygen evolution over perovskite by enhanced lattice oxygen participation, Nat. Commun. 11 (2020) 2002.

[35] J. Zhou, X. An, Q. Tang, H. Lan, Q. Chen, H. Liu, J. Qu, Dual channel construction of WO$_3$ photocatalysts by solution plasma for the persulfate-enhanced photodegradation of bisphenol A, Appl. Catal. B 277 (2020), 119221.

[36] L. Xu, Q. Jiang, Z. Xiao, X. Li, J. Huo, S. Wang, L. Dai, Plasma-engraved Co$_3$O$_4$ nanosheets with oxygen vacancies and high surface area for the oxygen evolution reaction, Angew. Chem. Int. Ed. 55 (2016) 5277–5281.

[37] L. Wan, Q. Zhou, X. Wang, T.E. Wood, L. Wang, P.N. Duchesne, J. Guo, X. Yan, M. Xia, Y.F. Li, A.A. Jelle, U. Ulmer, J. Jia, T. Li, W. Sun, G.A. Ozin, Cu$_2$O nanocubes with mixed oxidation-state facets for (photo)catalytic hydrogenation of carbon dioxide, Nat. Catal. 2 (2019) 889–898.

[38] D. Zhong, Z.J. Zhao, D. Cheng, B. Liu, G. Zhang, W. Deng, H. Dong, L. Zhang, J. Li, J. Li, J. Gong, Coupling of Cu(100) and (110) facets promotes carbon dioxide conversion to hydrocarbons and alcohols, Angew. Chem. Int. Ed. 60 (2021) 4879–4885.

[39] L. Kang, B. Wang, Q. Bing, M. Zalibera, R. Buchel, R. Xu, Q. Wang, Y. Liu, D. Gianolio, C.C. Tang, E.K. Gibson, M. Danaie, C. Allen, K. Wu, S. Marlow, L. D. Sun, Q. He, S. Guan, A. Savitsky, J.J. Velasco-Velez, J. Callison, C.W.M. Kay, S. E. Pratsinis, W. Lubitz, J.Y. Liu, F.R. Wang, Adsorption and activation of molecular oxygen over atomic copper(I/II) site on ceria, Nat. Commun. 11 (2020) 4008.

[40] M. Li, Y. Ma, J. Chen, R. Lawrence, W. Luo, M. Sacchi, W. Jiang, J. Yang, Residual chlorine induced cationic active species on a porous copper electrocatalyst for highly stable electrochemical CO$_2$ reduction to C$_{2+}$, Angew. Chem. Int. Ed. 60 (2021) 11487–11493.

[41] Y. Shang, L. Guo, Facet-controlled synthetic strategy of Cu$_2$O-based crystals for catalysis and sensing, Adv. Sci. 2 (2015), 1500140.

[42] L. Liu, W. Yang, W. Sun, Q. Li, J.K. Shang, Creation of Cu$_2$O@TiO$_2$ composite photocatalysts with p-n heterojunctions formed on exposed Cu$_2$O facets, their energy band alignment study, and their enhanced photocatalytic activity under illumination with visible light, ACS Appl. Mater. Interfaces 7 (2015) 1465–1476.

[43] A. Chen, X. Yu, Y. Zhou, S. Miao, Y. Li, S. Kuld, J. Sehested, J. Liu, T. Aoki, S. Hong, M.F. Camellone, S. Fabris, J. Ning, C. Jin, C. Yang, A. Nefedov, C. Wöll, Y. Wang, W. Shen, Structure of the catalytically active copper–ceria interfacial perimeter, Nat. Catal. 2 (2019) 334–341.

[44] J. Suntivich, W.T. Hong, Y.-L. Lee, J.M. Rondinelli, W. Yang, J.B. Goodenough, B. Dabrowski, J.W. Freeland, Y. Shao-Horn, Estimating hybridization of transition metal and oxygen states in perovskites from O K-edge X-ray absorption spectroscopy, J. Phys. Chem. C 118 (2014) 1856–1863.

[45] Y. Liang, Y. Li, H. Wang, J. Zhou, J. Wang, T. Regier, H. Dai, Co$_3$O$_4$ nanocrystals on graphene as a synergistic catalyst for oxygen reduction reaction, Nat. Mater. 10 (2011) 780–786.

[46] Y. Orikasa, T. Ina, T. Nakao, A. Mineshige, K. Amezawa, M. Oishi, H. Arai, Z. Ogumi, Y. Uchimoto, An X-ray absorption spectroscopic study on mixed conductive La$_{0.6}$Sr$_{0.4}$Co$_{0.8}$Fe$_{0.2}$O$_{3-δ}$ cathodes. I. Electrical conductivity and electronic structure, Phys. Chem. Chem. Phys. 13 (2011) 16637–16643.

[47] J. Yang, C. Yu, C. Hu, M. Wang, S. Li, H. Huang, K. Bustillo, X. Han, C. Zhao, W. Guo, Z. Zeng, H. Zheng, J. Qiu, Surface-confined fabrication of ultrathin nickel cobalt-layered double hydroxide nanosheets for high-performance supercapacitors, Adv. Funct. Mater. 28 (2018), 1803272.

[48] D. Wang, J. Zhou, Y. Hu, J. Yang, N. Han, Y. Li, T.-K. Sham, In situ X-ray absorption near-edge structure study of advanced NiFe(OH)$_x$ electrocatalyst on carbon paper for water oxidation, J. Phys. Chem. C 119 (2015) 19573–19583.

[49] K. Luo, M.R. Roberts, R. Hao, N. Guerrini, D.M. Pickup, Y.S. Liu, K. Edstrom, J. Guo, A.V. Chadwick, L.C. Duda, P.G. Bruce, Charge-compensation in 3d-transition-metal-oxide intercalation cathodes through the generation of localized electron holes on oxygen, Nat. Chem. 8 (2016) 684–691.

[50] Y. Zhao, Y. Zhao, R. Shi, B. Wang, G.I.N. Waterhouse, L.Z. Wu, C.H. Tung, T. Zhang, Tuning oxygen vacancies in ultrathin TiO$_2$ nanosheets to boost photocatalytic nitrogen fixation up to 700 nm, Adv. Mater. 31 (2019), e1806482.

[51] Y. Bai, J. Lu, H. Bai, Z. Fang, F. Wang, Y. Liu, D. Sun, B. Luo, W. Fan, W. Shi, Understanding the key role of vanadium in p-type BiVO$_4$ for photoelectrochemical N$_2$ fixation, Chem. Eng. J. 414 (2021), 128773.

[52] Y. Bai, H. Bai, Z. Fang, X. Li, W. Fan, W. Shi, Understanding the Z-scheme heterojunction of BiVO$_4$/PANI for photoelectrochemical nitrogen reduction, Chem. Commun. 57 (2021) 10568–10571.

[53] C. Wang, X.-D. Zhu, P.-J. Zuo, Novel confinement of Mn$_3$O$_4$ nanoparticles on two-dimensional carbide enabling high-performance electrochemical synthesis of ammonia under ambient conditions, Chem. Eng. J. 396 (2020) 125163.

[54] C. Wang, J. Gao, J.G. Zhao, D.J. Yan, X.D. Zhu, Synergistically coupling black phosphorus quantum dots with MnO$_2$ nanosheets for efficient electrochemical nitrogen reduction under ambient conditions, Small 16 (2020), e1907091.

[55] K. Chu, X. Li, Q. Li, Y. Guo, H. Zhang, Synergistic enhancement of electrocatalytic nitrogen reduction over boron nitride quantum dots decorated Nb$_2$CT$_x$-MXene, Small 17 (2021), e2102363.

[56] P.H. van Langevelde, I. Katsounaros, M.T.M. Koper, Electrocatalytic nitrate reduction for sustainable ammonia production, Joule 5 (2021) 290–294.

[57] H. Hu, S. Cai, H. Li, L. Huang, L. Shi, D. Zhang, Mechanistic aspects of deNO$_x$ processing over TiO$_2$ supported Co–Mn oxide catalysts: structure–activity relationships and in situ DRIFTs analysis, ACS Catal. 5 (2015) 6069–6077.

[58] H. Wang, H. Zhang, X. Li, J. Li, W. Cen, Q. Li, F. Dong, Highly enhanced visible light photocatalysis and in situ FT-IR studies on Bi metal@defective BiOCl hierarchical microspheres, Appl. Catal. B 225 (2018) 218–227.

[59] X. Deng, Y. Yang, L. Wang, X.Z. Fu, J.L. Luo, Metallic Co nanoarray catalyzes selective NH$_3$ production from electrochemical nitrate reduction at current densities exceeding 2 A cm^{-2}, Adv. Sci. 8 (2021) 2004523.

[60] X. Chang, X. Wang, Z.J. Zhao, P. Yang, J. Greeley, R. Mu, G. Zhang, Z. Gong, Z. Luo, J. Chen, Y. Cui, G.A. Ozin, J. Gong, Tuning Cu/Cu$_2$O interfaces for the reduction of

carbon dioxide to methanol in aqueous solutions, Angew. Chem. Int. Ed. 57 (2018) 15415–15419.

[61] S. Tang, Q. Dang, T. Liu, S. Zhang, Z. Zhou, X. Li, X. Wang, E. Sharman, Y. Luo, J. Jiang, Realizing a not-strong-not-weak polarization electric field in single-atom catalysts sandwiched by boron nitride and graphene sheets for efficient nitrogen fixation, J. Am. Chem. Soc. 142 (2020) 19308–19315.

[62] X. Li, Y. Luo, Q. Li, Y. Guo, K. Chu, Constructing an electron-rich interface over an Sb/Nb$_2$CT$_x$–MXene heterojunction for enhanced electrocatalytic nitrogen reduction, J. Mater. Chem. A 9 (2021) 15955–15962.

[63] R. Daiyan, T. Tran-Phu, P. Kumar, K. Iputera, Z. Tong, J. Leverett, M.H.A. Khan, A. Asghar Esmailpour, A. Jalili, M. Lim, A. Tricoli, R.-S. Liu, X. Lu, E. Lovell, R. Amal, Nitrate reduction to ammonium: from CuO defect engineering to waste NO$_x$-to-NH$_3$ economic feasibility, Energy Environ. Sci. 14 (2021) 3588–3598.

[64] M. Duca, N. Sacré, A. Wang, S. Garbarino, D. Guay, Enhanced electrocatalytic nitrate reduction by preferentially-oriented (100) PtRh and PtIr alloys: the hidden treasures of the 'miscibility gap', Appl. Catal. B 221 (2018) 86–96.

[65] T. Hu, C. Wang, M. Wang, C.M. Li, C. Guo, Theoretical insights into superior nitrate reduction to ammonia performance of copper catalysts, ACS Catal. 11 (2021) 14417–14427.

[66] C. Yang, Y. Zhu, J. Liu, Y. Qin, H. Wang, H. Liu, Y. Chen, Z. Zhang, W. Hu, Defect engineering for electrochemical nitrogen reduction reaction to ammonia, Nano Energy 77 (2020), 105126.

[67] J. Yang, P. Sebastian, M. Duca, T. Hoogenboom, M.T. Koper, pH dependence of the electroreduction of nitrate on Rh and Pt polycrystalline electrodes, Chem. Commun. 50 (2014) 2148–2151.

[68] G. Cioncoloni, I. Roger, P.S. Wheatley, C. Wilson, R.E. Morris, S. Sproules, M. D. Symes, Proton-coupled electron transfer enhances the electrocatalytic reduction of nitrite to NO in a bioinspired copper complex, ACS Catal. 8 (2018) 5070–5084.

[69] C. Xu, G. Chen, Y. Zhao, P. Liu, X. Duan, L. Gu, G. Fu, Y. Yuan, N. Zheng, Interfacing with silica boosts the catalysis of copper, Nat. Commun. 9 (2018) 3367.